Multicolor localization microscopy

by point-spread-function engineering

Yoav Shechtman[1], Lucien E. Weiss[1], Adam S. Backer[1,2], Maurice Y. Lee[1,3], and W.E. Moerner[1]

[1] Department of Chemistry, Stanford University, 375 North-South Mall, Stanford, California 94305, United States

[2] Institute for Computational and Mathematical Engineering, 475 Via Ortega, Stanford, California 94305, United States

[3] Biophysics Program, Stanford University, Stanford, CA 94305, United States

Supplementary Information

Contents

Optical setup and imaging model

In this section, we describe the imaging model used for maximum-likelihood estimation of the 3D position of the tetrapod PSFs used for dual-color particle tracking and/or fiducial-based imaging extended z-range. We detail how simulated images were generated, which were subsequently fit to raw data, in order to deduce the positions of emitters. Our simulation framework is identical to that used in ref. [1], and models the experimental system depicted in Fig. S1. We reproduce the relevant equations here for completeness and ease of reference.

Our simulation calculates the expected images of isotropic fluorescent emitters suspended above a water ($n_1 = 1.33$)/glass ($n_2 = 1.518$) interface. The emitter's depth is characterized by the distance between the emitter and the interface (z_1) and the distance between the emitter and the microscope focal plane (z_2) (see inset, Fig. S1 for schematic of coordinate system). The pupil phase function is:

$$\psi\left(u,v,z\right)=e^{ikn_1 z_1 \sqrt{1-u^2-v^2}+ikn_2 z_2 \sqrt{1-\frac{n_1}{n_2}\left(u^2+v^2\right)}}$$

(1)

In Eq. 1, pupil coordinates (x', y') are normalized with respect to the numerical aperture, such that the circle $\sqrt{u^2+v^2} = N.A./n_2$ lies on the outer edge of the pupil's region of support, and k is the wavenumber. The pupil electric field amplitude is determined from the following geometrical considerations: The objective lens collects a 'cone' of light-rays emanating from an emitter, and projects the spherical cap of collected rays onto a circle at the microscope pupil plane. Towards the edge of the microscope pupil, the spherical cap of rays undergoes a greater amount of compression when it is projected onto a two-dimensional circle. Hence, the edge of the pupil will contain the majority of light intensity. Quantitatively, the pupil intensity will exhibit a $U_{pupil} \propto cos^{-1}\left(\theta\right)$ dependence, where θ corresponds to a given polar angle at which rays are collected by the objective. The pupil electric field amplitude a will therefore be proportional to $cos^{-1/2}\left(\theta\right)$. This cosine apodization factor was originally developed in ref. [2] and has been often used for simulating high-N. A. optical systems (see, for example, equation 16 of ref. [3]). In Cartesian $\{u,v\}$ coordinates, the electric-field amplitude is expressed as:

3

$$a(u,v) \;=\; \begin{cases} \left(\dfrac{1}{1-u^2-v^2}\right)^{\frac{1}{4}} & If \;\; \sqrt{u^2+v^2} \leq n_1/n_2 \\[2mm] 0 & Otherwise \end{cases} \tag{2}$$

We limit the pupil support to the region containing subcritical light, within the circle $\sqrt{u^2+v^2} \leq n_1/n_2$. (Super-critical light will be severely attenuated for any emitter an appreciable distance from the interface, so this approximation is highly accurate.) The overall image-plane intensity distribution is thus determined to be [4]:

$$U(x,y) \propto \left| \iint a(u,v)\, p(u,v)\, \psi(u,v,z)\, e^{-i\frac{2\pi}{\lambda f}(ux+vy)}\, du\, dv \right|^2 \tag{3}$$

where $p(u,v)$ is the phase function imparted by the SLM, and f is the Fourier-transform lens focal length.
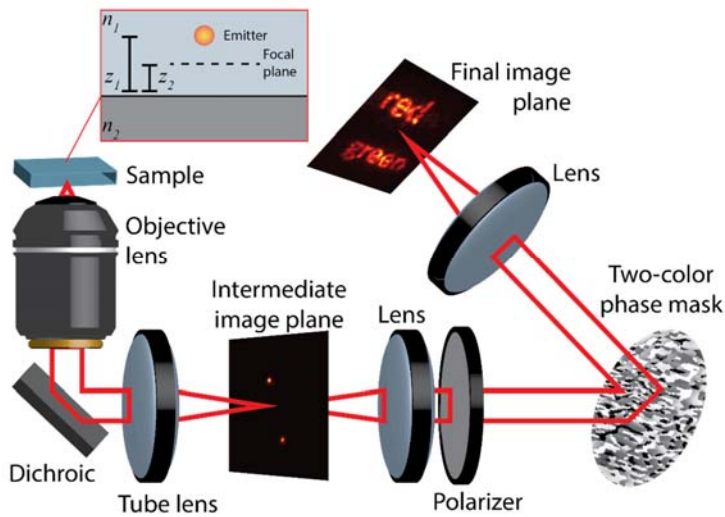
Supplemental Figure S1 | Experimental scheme.

4

SLM mask design algorithm

Given a set of N wavelengths $\lambda_i, i = 1 \dots N$ and N corresponding desired phase patterns $D(x,y)_i, i = 1 \dots N$, an SLM voltage pattern $V(x,y)$ is sought that minimizes the least squared phase distance between the all N desired phase patterns and the actual corresponding phase masks. The optimization is performed pixel-wise (namely separately for each one of the 512x512 pixels on the SLM). We therefore determine the voltage applied to each SLM pixel based on the following least-squares (LS) optimization problem:

$$v_{xy} = argmin \sum_{i=1}^{N} Dist_{2\pi} \left(P_i \left(v_{xy} \right), D_{xy,i} \right)^2$$
$$\text{s.t. } v_{min} < v_{xy} < v_{max}$$

(4)

where $P_i(v)$ is the phase delay that wavelength λ_i experiences when voltage v is set on the SLM pixel. This function is acquired by experimental calibration (See main text Fig. 1a and SLM calibration below). The constraint on the voltage v in Eq. 4 bounds it within the applicable input voltage range of the SLM. $D_{xy,i}$ is the desired phase value at pixel xy for wavelength λ_i. $Dist_{2\pi}$ denotes phase distance, namely:

$$Dist_{2\pi} \left(a,b \right) = 2\pi \cdot \left| \frac{a-b}{2\pi} - \left[\frac{a-b}{2\pi} \right] \right|$$

(5)

where $[\cdot]$ denotes the nearest integer, or 'round' operator.

Several modifications to the basic LS problem (Eq. 4) are performed in this work. First, note that for a single wavelength, a desired phase pattern can have any constant phase added to all of its pixels, with no effect on the PSF. However, such a constant changes the resulting voltage pattern (Eq. 4). Therefore, this is an additional degree of freedom to optimize: a constant phase α_i in the range $[0,2\pi]$ is added to each design pattern $D(x,y)_i$.

Secondly, a possibility to demand a 'closer match' with certain wavelengths is added. This is because in certain applications, some wavelengths may be more important than others. For example, in the 3D super-resolution imaging demonstration performed in this work (SI section "3D super resolution imaging of thick specimens", Figure S10), the red PSF corresponds to single

5

molecules, whereas the green PSF corresponds to the fiducial, which is much brighter. Therefore, in order to optimize localization precision, the red PSF (astigmatism) is weighed more strongly.

The general problem we solve in order to find a voltage pattern is therefore:

$$v_{xy} = argmin \sum_{i=1}^{N} w_i \cdot Dist_{2\pi} \left(P_i \left(v_{xy} \right), D_{xy,i} + \alpha_i \right)^2 \tag{6}$$

Where w_i is the relative weight of wavelength λ_i.

Figure S2 shows the mask designed and used for the 2D super-resolution imaging experiment (main text Fig. 4). For the green label (Alexa 532, $\lambda = 555\ nm$) it yields a laterally shifted standard PSF in the X direction. For the red label (Alexa647, $\lambda = 673\ nm$), it is a standard PSF shifted in the Y direction. The actual voltage map is shown in Fig S2a, and the desired phase masks for green and red are shown in Fig S2b and S2d respectively. The actual phase delays experienced by red and green colors are shown in Fig S2c and S2e. For this mask design the parameters are $\lambda = (538,673)\ nm$ and $w = (1,1)$.
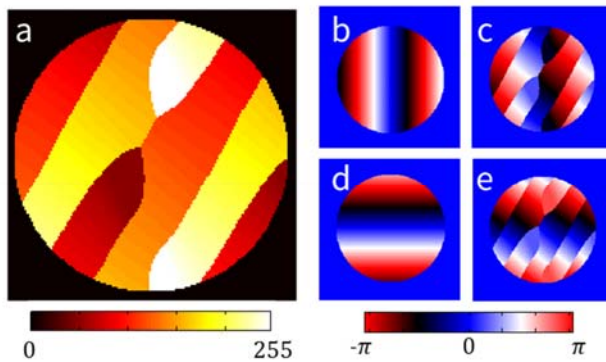
Supplemental Figure S2 | Orthogonal shift mask. a, SLM Voltage pattern. **b**, desired phase mask for green (horizontal shift). **c**, Actual phase pattern experienced by green. **d**, desired phase mask for red (vertical shift). **e**, Actual phase pattern experienced by red.

Note that the cost function has a hard limit on the voltage. Generally, the solution has a small preference towards values at the limits of the SLM. For example, ~ 6% of the SLM pixels on the dual-color 20 μm Tetrapod mask used in the 3D diffusion measurements are at the top or bottom value out of 256 possible SLM voltages.
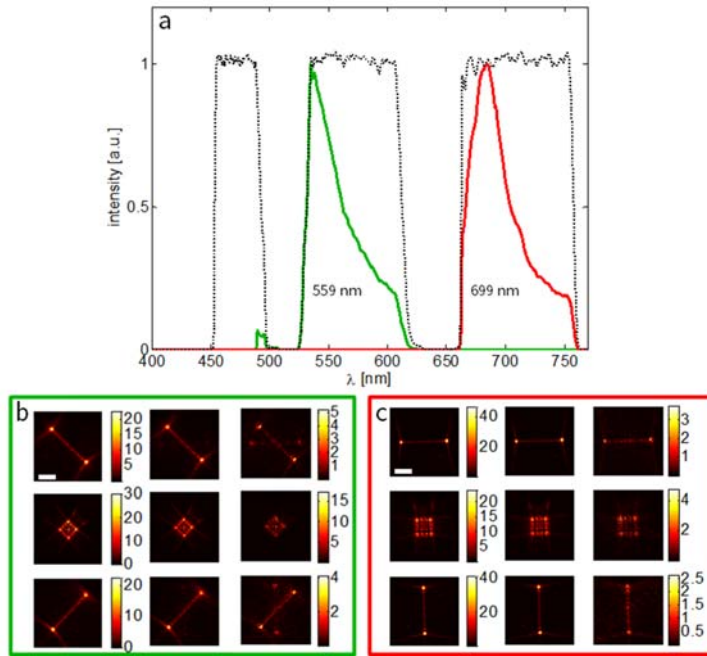
Effect of emitter spectral width

Our design algorithm optimizes a phasemask at specific wavelengths with infinitely narrow bandwidth. In practice, fluorescent emitters have emission spectra of finite bandwidth, and in our implementation we select the mean emission wavelength of an emitter as the design wavelength. The mask design appears to be robust to this effect, as a comparison between the numerically calculated PSFs and the experimentally measured ones indicate (e.g. main text Fig. 2).

To further appreciate the effect of spectral width on the performance of the mask, we investigate numerically the PSFs of the two fluorescent microspheres used in this work. Specifically, we compare the PSFs obtained by using the full emission spectrum of each of the microspheres (accounting for the experimentally used filters, simulation performed by a series of narrow band calculations at every 10 nm and summing), with the PSFs obtained by a spectrally-narrow emitter with the same mean wavelength. The extent of the spectral width effect will depend on the specific mask design and implementation parameters: spectral distance between emitters, dynamic range of SLM, etc. In this section we investigate one of the masks used in the work: the dual-color 20 μm Tetrapod mask (main text Fig. 2).

Figure S3 shows the result of this comparison. The PSFs of spectrally narrow emitters (left) are compared to those of emitters with the full spectra (middle), for 3 defocus positions (-10,0,10) μm. Taking the full spectrum into account does not change the PSF significantly, although for the green microsphere, some 'PSF-leakage' from the red PSF is apparent, as is most visible in the absolute difference image (Fig. S3b, right).

While the finite-spectrum effect is not of considerable significance in this case of spectrally well separated emitters, such considerations can be incorporated in the mask design algorithm in the future in order to improve performance in more challenging cases.

Supplemental Figure S3 | Effect of spectral width of emitter. a, Emission spectrum of green and red microspheres (in green and red), accounting for filter transmission (dotted black). **b (c),** Calculated PSF for green (red) microsphere. Left: assuming a narrow source of 559 nm (699 nm), middle: Using the full spectrum. Right: Absolute difference between left and middle with appropriate color scale. Three defocus (z) levels are used: -10 µm (top), 0 (center),10 µm (bottom). Color scale is in arbitrary units, and consistent for each pair of narrow/full spectrum PSFs. Scale bars are 5 µm.

Sensitivity to emitter wavelength

The robustness of the mask's design to mismatch between the design wavelength and the actual mean wavelength of the emitter is of practical importance, and could also provide insight as to the limitation of the method in terms of minimum spectral separation of emitters. Here we present simulation results for the 2 color 20 µm Tetrapod PSF used in this work, however a detailed investigation should be made for each different design. Figure S4 shows the numerically calculated PSF for different emitter wavelengths (assumed to be very spectrally narrow). The phase vs voltage dependence of the SLM for different wavelengths is calculated by a linear

interpolation between the calibrated wavelengths (see SI section "SLM calibration"). The intensity is scaled the same in all figures, showing that the PSF becomes dimmer as well as distorted, as the wavelength deviates from the design wavelengths, which are 559 nm and 699 nm. Nevertheless the design seems fairly robust to the emitter wavelength.
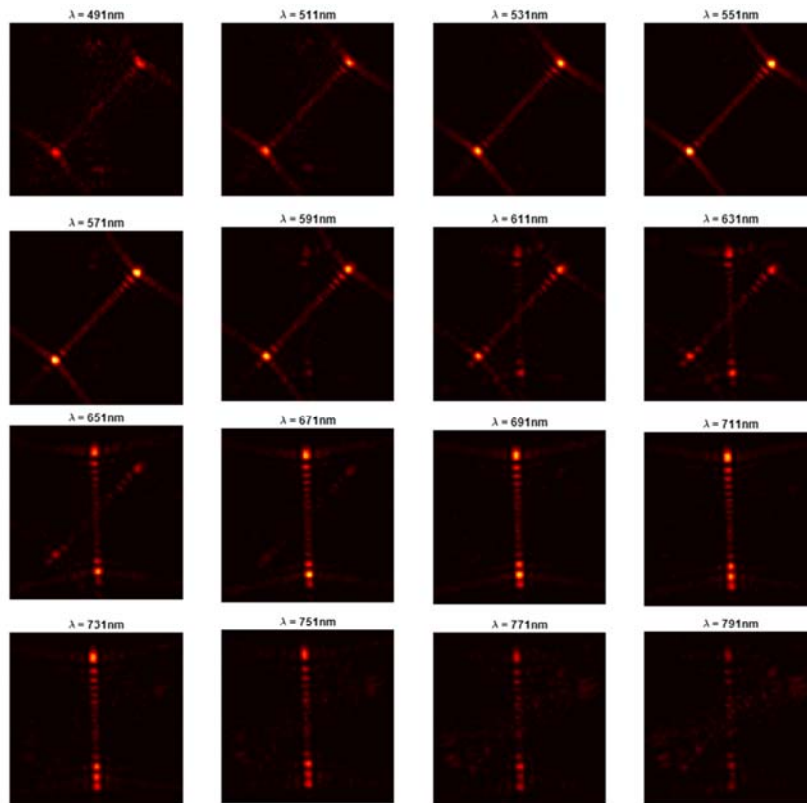

Supplemental Figure S4 | Sensitivity to emitter wavelength.

Minimal spectral separation of two emitters

The next natural question is – **How spectrally close can the design wavelengths be for a multicolor mask to produce controllably different PSFs**? The answer to this depends on the number of different wavelengths, the specific PSFs the implementation method, and the design

algorithm. Considering a concrete example of designing a 20 μm Tetrapod rotated by 45 degrees for 2 wavelengths in our LC-SLM, we can answer this question by numerical simulation.

Figure S5 shows the resulting calculated PSFs (for an emitter defocused by 9 μm) for a multicolor mask designed for 2 wavelengths at varying spectral separations around a mid wavelength of 610nm. Significant cross-talk starts becoming noticeable for a spectral separation smaller than ~60 nm (580,640 nm and closer). This limitation ultimately comes from the limited spectral dispersion of the LC-SLM. In many regards, using a dielectric mask for a multicolor PSF promises much better performance, as demonstrated in SI section "Dielectric multicolor mask".
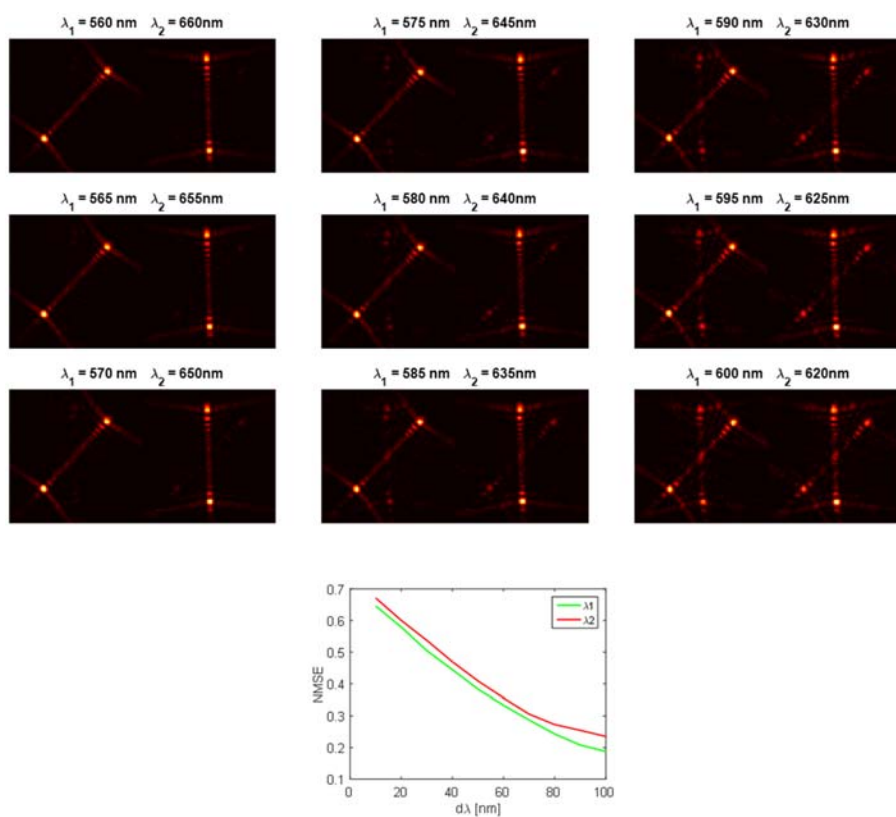
Supplemental Figure S5 | Effect of design wavelengths proximity. Calculated PSF pairs as a function of wavelength separation (top) and normalized mean squared error (NMSE) between designed PSFs and resulting PSFs for both colors (bottom).

SLM calibration

In this section, we describe an image-based calibration procedure for determining the phase response of the SLM at multiple wavelengths. Calibrations detailed in this section were used to generate the phase versus voltage plots shown in Fig. 1a (main text). While simple interferometry setups [5] may alternatively be used to calibrate the SLM, such approaches require one to approximate the true emission spectra of the fluorescent dyes used in imaging experiments with coherent light from lasers chosen to have similar mean wavelength, but which have much narrower spectra. Additionally, the method detailed in this section does not require any hardware reconfiguration of the experimental system used for imaging. Two separate calibrations were performed using sub-wavelength fluorescent beads with emission spectra that closely matched the two color spectra used for imaging experiments. After accounting for the pass bands of the emission filters, the two types of fluorescent beads had center-of-mass emission wavelengths of 559 nm and 699 nm.

The SLM was programmed with a sequence of 'grating' phasemasks, in which each period of the grating contains two separate voltage settings. For each phasemask loaded onto the SLM, an image of a bead is acquired. Each time a new phasemask is loaded onto the SLM, the peak intensity of the bead will change as a function of the two voltages applied within the grating phasemask. The image plane intensity distribution associated with an isotropic point source is then given by Eq. 3. However, say we wish to determine the image-plane intensity at point $(0,0)$, and we image an emitter placed on the coverslip, in perfect focus (i.e. $\psi(u,v,z)=1$). In this case, Eq. 3 simplifies to:

$$U(0,0) \propto \left| \iint a(u,v) p(u,v) du dv \right|^2 \tag{7}$$

We now write the explicit formula for the grating phasemask p as:

$$p(u,v) = \begin{cases} 1 & \text{if } \mod[u,u_0] \leq u_0/2 \\ e^{i\delta} & \text{if } \mod[u,u_0] > u_0/2 \end{cases} \tag{8}$$

11

Where u_0 is the grating period, and δ is the phase difference resulting from the two distinct voltages applied upon the SLM. Substituting Eq. 8 into Eq. 7, moving constant terms outside of the integral and simplifying, we arrive at the following expression for $U(0,0)$:

$$U(0,0) \propto (1+cos(\delta)) \sum_{i=0}^{N} a_j \qquad (9)$$

Where: $a_j = 2 \int_{-\infty}^{\infty} \int_{j \times u_0}^{j \times u_0 + \frac{u_0}{2}} a(u,v) du\, dv$, and N is determined by the number of grating periods required to fill the width of the microscope pupil. In deriving Eq. 9, we have also used the fact that the pupil amplitude associated with a point source is symmetric, i. e. $a(u,v) = a(-u,v)$. The SLM pixels may be programmed with one of 256 discrete voltage settings. In order to determine the phase response of a given voltage, a sequence of 256 phasemasks is chosen in which the voltage in one half of the grating period is held constant at a setting of 127 and is referred to as the 'reference voltage', while the voltage in the other half of the period is varied from 0 to 255 for each separate phasemask, and is referred to as the 'test voltage'. Each grating pattern had a period of 32 SLM pixels. For the image corresponding to j 'th grating phasemask, a quantity proportional to $U(0,0)$ is computed by summing the ADC counts of the brightest five camera pixels in the image, and is referred to as U_j. After a sequence of 256 images is acquired, the brightest and dimmest values of U_j are determined (U_{max} and U_{min} respectively), in addition to the amplitude of the variation in intensity: $A = U_{max} - U_{min}$. The relative phase difference, δ_j, between the reference and test voltage for the j 'th grating pattern is determined as:

$$|\delta_j| = cos^{-1} \left(\frac{U_j - U_{min} - A/2}{A} \right) \qquad (10)$$

To demonstrate the working principle of our method, Fig. S6a shows representative raw calibration data taken using a fluorescent bead with a mean emission wavelength of 559 nm. To minimize photobleaching, data was acquired at laser powers 5-10% of that used during imaging experiments, with a high EM gain of 300. As predicted, when different grating patterns are displayed on the SLM, the peak intensity of the bead grows brighter or dimmer. Also visible from

the raw data, are the first diffraction orders associated with the SLM grating pattern, which also oscillate sinuosoidally as a function of the phase difference between the reference and test voltage (albeit at a π phase offset). Hence, intensity measurements from the first diffraction order may interchangeably be used to calibrate the SLM. In Fig. S6b, measured values of U_j are plotted as a function of the 256 test voltages applied on the SLM. Intensity measurements from the zeroth and first diffraction orders are shown on separate plots, verifying the π phaseshift between the two sets of measurements. As expected, U_j varies sinuosoidally with respect to the test voltage. By counting the number of peaks and minima appearing in the raw data, we immediately conclude that the total modulation range of the SLM must be close to 5π for 559 nm light, and 4π for 699 nm light. However, we also observe that the peak intensity (achieved when the test voltage is equal to the reference voltage at setting 127) is not attained at the other peaks appearing in the data – a feature not predicted by Eq. 9. We ascribe this effect to the broadness of the emission spectra of the fluorescent bead: Only when the test voltage is equal to the reference voltage will all spectral components of the bead's emission be completely in phase. In order to compensate for this effect, instead of computing a single maxima U_{max} and modulation amplitude A, we compute a sequence of local modulation amplitudes A^k, and amend Eq. 10 to:

$$\left|\delta_j\right| = cos^{-1}\left(\frac{U_j - U_{min} - A^k/2}{A^k}\right) \tag{11}$$

in which we choose A^k according to which local maximum the j'th voltage setting is nearest. More sophisticated interpolation strategies can be explored, but we found the above data-processing strategy to be accurate enough for our purposes. In practice, intensity measurements from the zeroth diffraction order were used to calibrate the SLM at 559 nm, while the first diffraction order was used to calibrate the SLM at 699 nm, since a greater number of intensity maxima appeared in the first diffraction order data, leading to a more accurate calibration. Once a sequence of phase-difference measurements $\left|\delta_j\right|$ was computed, the phase was unwrapped, and the sign of each $\left|\delta_j\right|$ was determined based on the knowledge that the absolute phase lag monotonically increases with higher SLM voltage settings. The unwrapped phase measurements were then smoothed using a moving average filter of a span of eight sequential measurements, using a MATLAB built-in

function. In order to produce our final calibration curves, the phase measurements were then offset such that a voltage setting of 0 corresponded to zero relative phase lag.
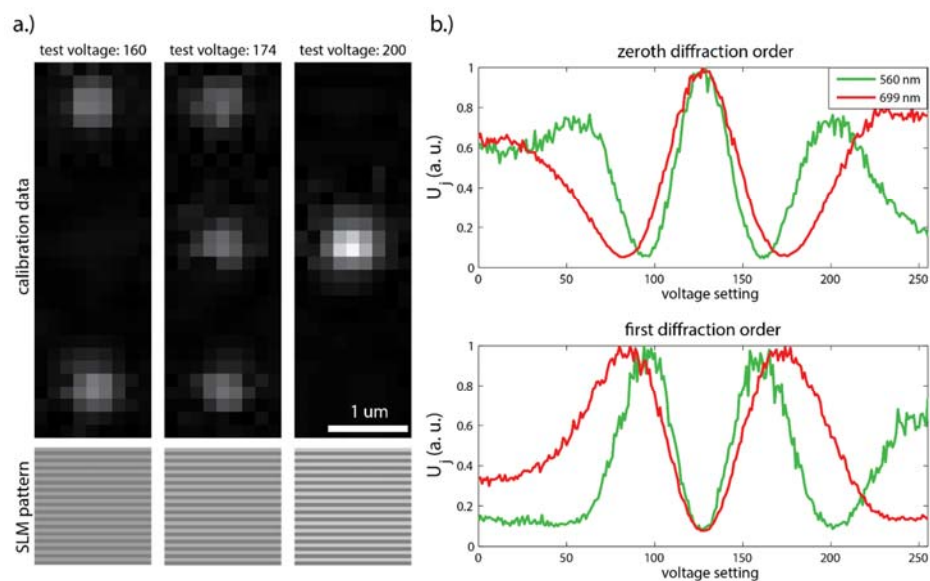

Supplemental Figure S6 | SLM calibration. a, Representative calibration images of a fluorescent bead (mean emission wavelength of 559 nm). Insets show the grating patterns used to induce the acquired images (gray levels denote different voltage settings, the test voltage settings were 160, 174 and 200, right to left. In all cases, the reference voltage setting was 127). Note the first diffraction orders, which also vary sinuosoidally in intensity, as a function of the applied voltage settings. **b,** Normalized plots of U_j versus applied voltage for the two separate color calibrations.

There are fewer peaks in the 699 nm calibration data, due to the fact that a fixed optical path length will induce a smaller phase lag for light of a longer wavelength. Both zeroth and first diffraction order data is plotted.

Multicolor registration

Due to the wavelength dependence of the phase mask, as well as additional chromatic aberrations in the setup, the resulting PSFs of different colors can be laterally shifted relative to one another. To account for this effect, color registration calibration measurements are performed. For this we

use a nanohole array, consisting of regularly spaced 200 nm diameter holes in a 100 nm thick Aluminum layer deposited on a glass cover slip [6].

On top of the nanohole array we place a droplet of water containing Alexa 647 dye and Atto 532 dye (spectrally extremely similar to Alexa 532) at ~100 μM concentration. We use two lasers (641 nm and 488 nm) to excite the sample sequentially. The absorption ratio for Atto 532 between 488 nm and 641 nm pumping is very large (>100) and for Alexa 647 is very small (<0.01). This means that effectively we can control the shape of the PSF produced by the nanohole array by using only one excitation laser at a time. Figure S7 shows the emission spectrum of Alexa 532 and Alexa 647 taking into account the filters in our setup.
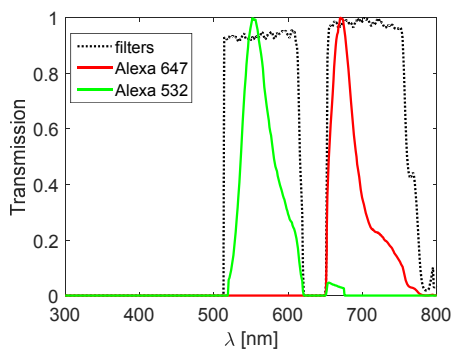

Supplemental Figure S7| Emission spectrum of Alexa 532 and Alexa 647 and dichroic mirror transmission

We first illuminate this sample with a red laser (641 nm). This produces an array of red PSFs in the image plane, and we measure 100 frames at 20Hz. We then illuminate with a 488 nm laser producing an array of green PSFs, and we measure another 100 frames at 20Hz. We then localize all points in all frames using the center of the 2D Gaussian fit. The resulting localizations are shown in Fig. S8.

The mean green-red displacement over the field of view is calculated by sub-pixel cross-correlation to be [70, -2] nm in the [x,y] direction, and this correction is applied to the super-resolution data. The localization precision of each point source obtained by the standard deviation of the 100 frames of each color is estimated to be <1nm for green and <2.5 nm for red.

15

This measurement procedure constitutes a general color-registration method that can (and should) be performed for different dyes and different masks. Naturally, registration can be improved, e.g. performing local rather than global registration by interpolating the shift map, or performing 3D registration [6].
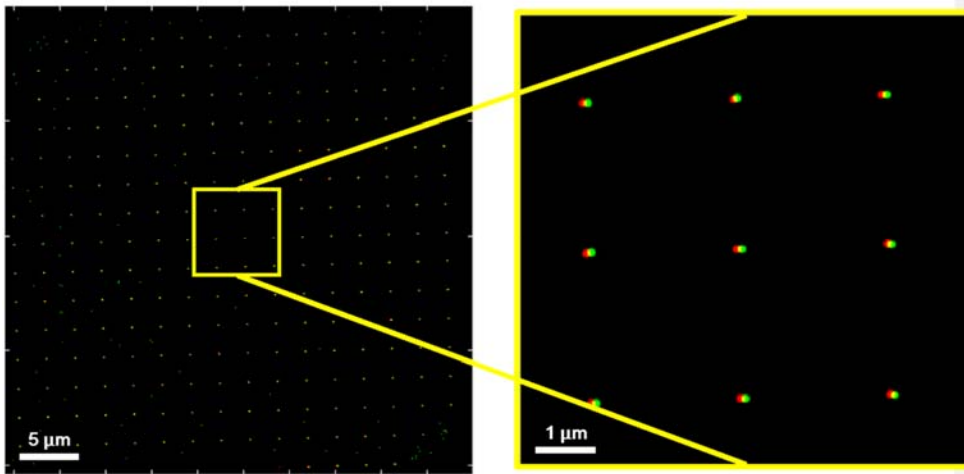
Supplemental Figure S8| Multicolor registration using nanohole array. Both red and green PSFs are localized using a nanohole array containing both Alexa 647 and Alexa 532 dyes. The distribution of localizations for 100 frames of each color are shown (zoom in on 9 nanoholes on the right).

Overlapping PSFs

PSFs designed for 3D localization are typically larger than the standard PSF, since they must encode the depth position in a 2D diffraction-limited intensity pattern. Therefore, the PSFs of proximal emitters, for example due to high emitter density or due to tracking interacting biomolecules, will overlap, and overlapping PSFs can make fitting a more challenging task. Note that the emitter overlap problem is not unique to the PSFs presented in this work. It is a general problem in localization microscopy, and in fact a rate limiting factor even in 2D localization microscopy, as it poses a limitation on the maximal density of "on" emitters per frame. Yet, due

to the larger size of the 3D PSFs, the problem is more acute in 3D localization applications. There are several possible approaches for dealing with this problem.

One solution is to fit detected PSFs as usual, and treat the overlapping ones as background noise. While this approach is simple to implement, it entails compromised localization precision and accuracy (See discussion in SI of Ref. [1]).

A different, more sophisticated approach would be to include more prior information on the image. For example, knowledge of the blinking statistics [7], or sparsity of emitters, both can be used to develop a solution for solving the overlap problem. Sparsity, in this context, means that within a region of interest where fitting is performed, it is no longer assumed that only one source is emitting, but rather that a *small* (unknown) number of sources are emitting, and that the signal in the region of interest consists of their overlapping PSFs. Then, one can use algorithmic approaches for solving sparse inverse problems. This approach has been suggested in the context of 2D [8-10] and 3D imaging [11, 12]. Extending these methods to engineered PSFs would be an exciting future research direction that should yield improved performance.

Finally, we consider another type of solution, using a concrete example with a specific (but reasonable) type of prior knowledge. This is the problem of tracking a pair of emitters in 3D that are known to be in close proximity. This can be the case of interacting biomolecules, each labeled with a different color in order to tell them apart. Using a multicolor Tetrapod PSF, the PSFs of these emitters will overlap. However, with a simple fix – namely, adding a linear phase ramp to one color – the PSF of that color can be shifted laterally significantly, such that the PSFs do not overlap, and localization is improved. Then, using a standard multicolor registration calibration measurement, this shift can be accounted for in post-processing.

Figure S9 shows a demonstration of this color-dependent shifting approach, using experimental measurements of two differently colored fluorescent microspheres. Simply applying a multicolor tetrapod PSF yields two closely spaced PSFS. However, applying a design based on the same multicolor mask but with a linear phase ramp added only to one color - red, shifts only that color laterally, with practically no effect on the other color (green), and no cost in terms of measured signal photons.
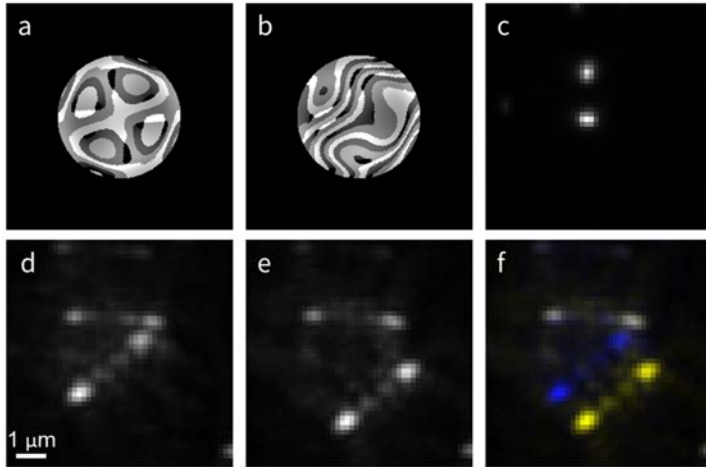
Supplemental Figure S9 | Single color lateral shift. a, A 6 μm Tetrapod multicolor voltage mask, rotated by 45 degrees. **b**, Voltage mask for the same 6 μm Tetrapod mask but with linear phase added to red. **c**, Experimentally measured image of two in focus fluorescent microspheres (green – top, red – bottom) with SLM turned off. **d**, Experimentally measured image of the same two microspheres, defocused by 2 um, using the voltage mask in **a**. **e**, Experimentally measured image of the defocused microspheres, using the voltage mask in **b**. The red microsphere appears to be shifted diagonally, while the green microsphere is unaffected. This is seen clearly in **f**, where images **d** and **e** are superimposed, in blue (**d**) and yellow (**e**) color scale, in which gray means overlap.

Overlapping PSFs – numerical investigation

The overall effect of PSF overlap on image quality is dependent on many different factors. We approximately quantify this by eliminating many experimental variables, using numerical simulation, as follows.

A set of N emitters is randomly placed in a $(6 \ \mu m)^3$ cube in object space. The emitters are then imaged using a 6 μm Tetrapod PSF, and the 3D position of each emitter is determined. As mentioned above, there are several possible algorithmic ways to deal with fitting overlapping PSFs. Here we choose the simple approach of using correlation against a dictionary to coarsely find PSFs, fitting each PSF (using MLE), while ignoring the existence of others, and then subtracting the localized emitter from the image, fitting the next one, and so on, until there is no likely fitting candidate in the image.

An example simulated image with N=5 is shown in Fig. S10, along with the PSFs that were fit at each stage. In the example frame shown in the figure, the mean 3D localization error for the 5 emitters was 36 nm. The number of signal photons per emitter is 20000, with a uniform background of 4 photons per pixel, and the noise is assumed to be Poisson. For each N, the localization is repeated 50 times to allow determination of average localization precision.
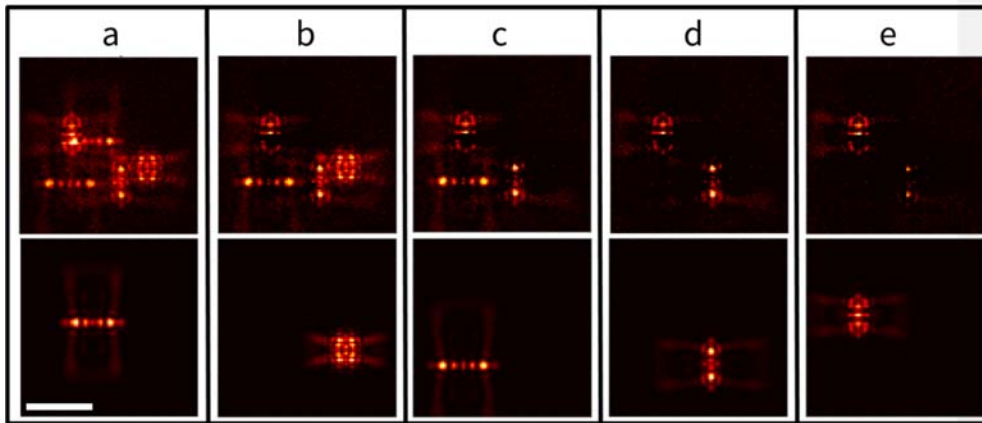

Supplemental Figure S10 | Simulation: fitting overlapping emitters. a, Top: Simulated image with 5 emitters in a $(6 \ \mu m)^3$ box. Bottom: First fit emitter. **b-e,** Top: image after subtracting the previous fit emitter. Bottom: Current fit emitter. Scale bar = 5 μm.

Naturally, increasing N degrades localization performance. Not only does localization precision suffer, but also some emitters can be non-localized (false negatives), where on the other hand fits can be made to nonexistent emitters (false positives). Figure S11 shows a quantification of localization performance as a function of N, in terms of a) percentage of acceptable localizations, defined as emitters localized to a precision better than 100 nm, and b) mean precision of these 'good' localizations. Values are shown for two SNR levels: signal photon number of 20k and 2M, both with a background of 10 photons per pixel.

While localization performance improves with more photons, the drastic effect of overlapping emitters is apparent. For example, the mean localization precision of 2 emitters within the $(6 \ \mu m)^3$ cube in object space, each with 2 Million signal photons, is already worse than a single emitter with 20 thousand signal photons (Fig. S11 b).

We note that these simulation results should serve as a rough estimate for attainable performance, and that better algorithms for dealing with overlap are expected to improve these results, possibly greatly. In addition, factors not accounted for in this simulation, e.g. model-mismatch, can have a significant effect on the results as well.
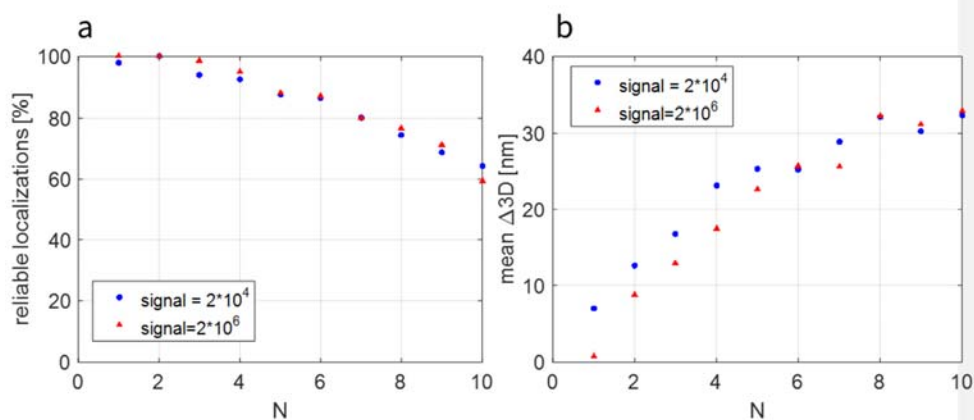

Supplemental Figure S11 | Overlapping emitters. a, Percentage of reliable localizations, defined as 3D localization error<100nm, vs. *N*. **b,** mean precision of reliable localizations vs. *N*.

3D super resolution imaging of thick specimens

As another demonstration, we combine 3D imaging in one color channel with localization of a fiducial for drift correction in the other color channel, thus facilitating 3D super-resolution imaging of a thick (~6 μm) specimen. We image the microtubules of fixed HeLa cells, immunolabeled with Alexa647 (a red fluorescent dye). The scheme works as follows: A fiducial, namely, an immobilized bright point source (a green fluorescent microsphere), is positioned near the cell. While PALM/STORM super-resolution imaging of the cell produces a sequence of images of blinking labels as usual, the fiducial's position is simultaneously recorded and used in post processing to determine the z position (and remove any drift) of the blinking labels at each frame. The PSF design consists of a 6 μm range Tetrapod in green (for the fiducial) and a short-range astigmatic mask in the red (for weak single-molecule emitters in a thin plane).

The result of this method is shown in Fig. S12: the fiducial in this example has been endocytosed by the cell, and is located ~3.5µm above the bottom of the cell. Microtubules are imaged both on the top of the cell (Fig. S12b and S12e) and on the bottom (Fig. S12c and S12f) – layers separated by up to 6µm. This is achieved simply by focusing the objective at different depths to place the astigmatic response where needed (The dark nucleus helps to limit out-of-focus fluorescence.) As the microsphere is a bright object, it is localized to an estimated precision of (10 nm, 8 nm, 13 nm) in (x,y,z), obtained by static localization measurements (see SI section "Experimental precision estimation"). We note that the 3D images are a bit spotty, and this is likely due to the premature photobleaching of labels which are illuminated but not imaged because they are far away from the imaging plane. This problem can be alleviated if light sheet illumination is used, for example.
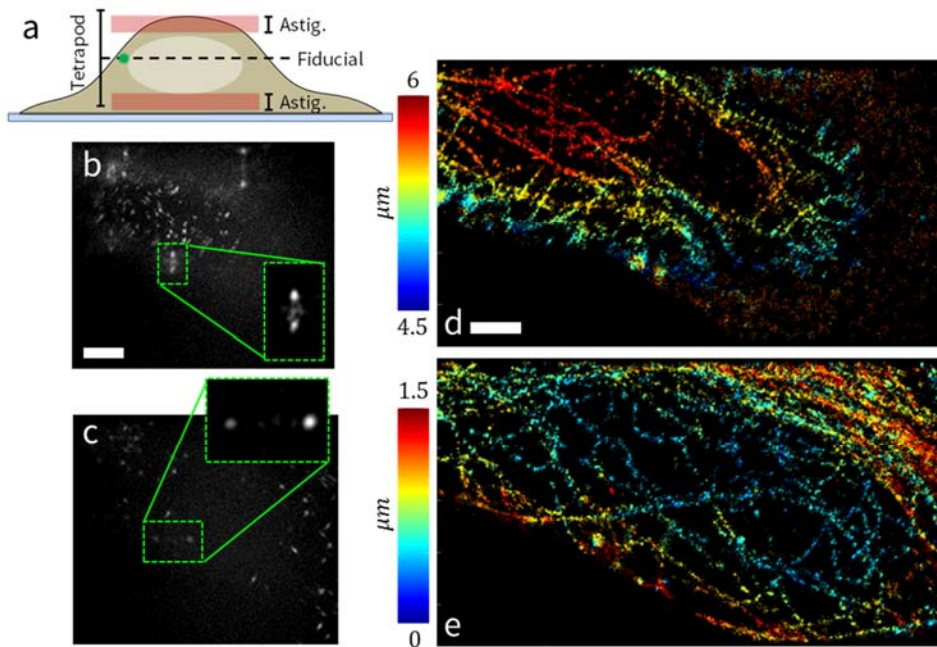

Supplemental Figure S12 | 3D super-resolution imaging of a ~6 µm thick cell using a distant fiducial. a, Cartoon diagram depicting the experimental setup: Super-resolution image of a cell was acquired by fluorophore blinking. Two focus regions are shown – above the nucleus, and below it. Throughout the cell (bottom to top) the fiducial is visible. **b (c)**, Example blinking data

acquired while focusing on top (bottom) of cell. The fiducial microsphere is marked in a dotted green rectangle. In green insets – expansion of the fiducial region averaged over 200 frames, for clarity. Scale bar = 5 μm. **d,** Super resolution image of top part of the cell (z=4.5 - 6 μm). Scale bar = 2 μm. **e,** Super resolution image of bottom part of the cell (z=0 – 1.5 μm). See also supplementary video 2.

The key novelty of this approach is the fact that the fiducials and labels have extremely different PSFs, even though the same optical pathway is used to image both simultaneously. Since the two probes have different spectra, they each interact with the SLM uniquely. As a result, one gets the 'best of both worlds': A large z-range PSF for the bright fiducial, and a small and accurate PSF for the dimmer labels. Of course, since both colors illuminate the camera, attention to the spectral properties of the emitters and sample is important: for example, emission (or background) leakage from one emitter class into the wavelength window of the other class should be minimal.

Figure S13 shows the mask design that was used for 3D super-resolution imaging of thick samples (Fig. S12). For the green fiducial (green, $\lambda = 559\ nm$) it yields a 6μm z-range Tetrapod PSF [1]. For the tubulin label, Alexa647 (red, $\lambda = 673\ nm$), it is astigmatic. The actual voltage map is shown in Fig S11a, and the desired phase masks for green and red are shown in Fig S11b and S11d respectively. The actual phase delays experienced by red and green colors are shown in Fig S11c and S13e. For this mask design the parameters are $\lambda = (559,673)\ nm$ and $w = (1,1.8)$.
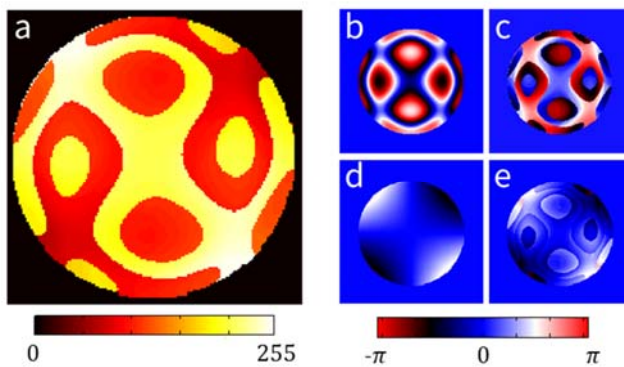
Supplemental Figure S13 | Tetrapod/Astigmatism mask. a, SLM Voltage pattern. **b**, desired phase mask for green (a 6μm z-range Tetrapod). **c**, Actual phase pattern experienced by green. **d**, desired phase mask for red (astigmatism). **e**, Actual phase pattern experienced by red.

The resulting PSFs, at various defocus levels are shown in Fig. S14, measured experimentally. The green point source is a 100nm 505/514 fluorescent microsphere. The red point source is a 200nm diameter hole in a 100nm thick aluminum layer, deposited on a glass cover slip, filled with Alexa647 dye.
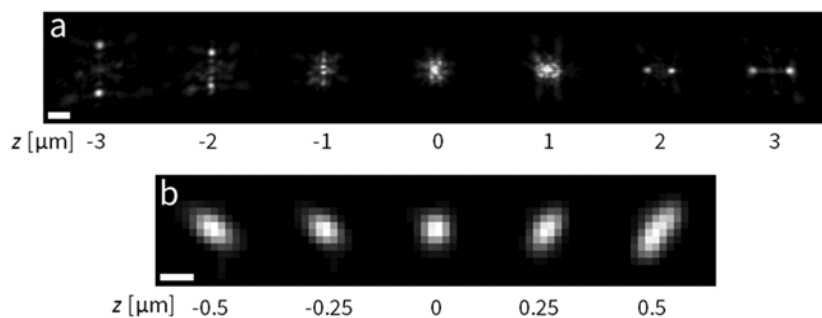
Supplemental Figure S14 | Tetrapod/Astigmatism PSF. a, A green fluorescent microsphere imaged throughout a 6 μm defocus range with the voltage mask shown in Fig. S11a. Scale bar=2 μm. **b,** A nanohole filled with Alexa647 molecules imaged over a 1 μm range using the same voltage mask. Scale bar = 0.5 μm.
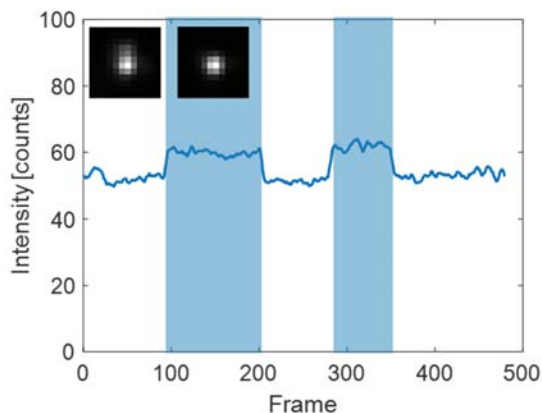
Mask efficiency

A multicolor mask obtained by solving a least-squares problem, is a compromise between several different desired masks - one for each color. Since the designed phase masks do not correspond identically to the desired masks (due to limited dynamic range of the SLM phase-voltage response), the PSFs will also deviate from the desired PSF. This can cause a difference in performance (e.g. attainable precision) between a 'single-color' PSF and a 'multi-color' PSF.

In general, the extent of this effect will depend on the exact desired patterns, and on the phase/voltage/wavelength relations of the SLM. To quantify this effect in our experiment, we perform several measurements. First, we compare the number of signal photons detected with a standard PSF with the number detected from the shifted PSF used in the cell experiment (main text Fig. 4).

As a point source we use a 200 nm diameter hole in a 100 nm thick Aluminum layer deposited on a glass cover slip [6]. A droplet of Alexa647 fluorophores is placed over the hole (~100 µM in water), such that the emitters within the hole are constantly replaced, and the intensity is approximately constant over time.

Figure S15 shows intensity measurements in a 12x12 pixel region around the emitter. The LC-SLM containing the multicolor mask is toggled on and off, and the intensity in each frame is shown, after background subtraction. . The ratio between the mean "mask-on" state (left inset, white regions) and "mask-off" (right inset, blue regions) is 0.864, corresponding to a 'cost' of 13.6% in signal photons due to the imperfect modulation mentioned above.
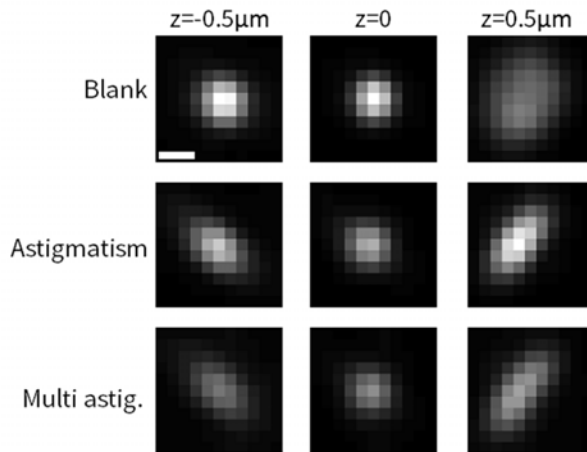

Supplemental Figure S15 | Mask efficiency – standard PSF vs. shifted.

Next, we compare the performance of a single astigmatic PSF to the multicolor PSF used in the 3D super-resolution imaging experiment in the previous SI section (i.e. red = astigmatism, green = 6 µm Tetrapod). First, we give some quantification of the brightness of a single color mask vs. a multicolor mask.

Three defocused images under the same pumping conditions are shown in Fig. S16, for three different SLM patterns: a constant pattern (blank) on the SLM, a single color astigmatic PSF, and the multicolor astigmatic PSF. Comparing the total number of photons in a 11x11 pixel box in all three defocus levels between the three SLM patterns yield a ratio of 1:0.95:0.83, implying

24

that the 'cost' in terms of photon counts of adding another color to this specific PSF is a loss of $1 - \frac{0.83}{0.95} \cong 13\%$.

Supplemental Figure S16 | PSF efficiency: Blank mask, single color astigmatism and multicolor astigmatism. Experimental measurements of the PSF. The point source is a nanohole filled with Alexa647. Three defocus levels are imaged (-0.5um, 0, +0.5um) for no mask (top), single color astigmatism (middle) and multicolor astigmatism (bottom). Scale bar = 500nm.

To quantify mask efficiency further, we perform a measurement with a more practical result, namely, a comparison between the expected precision of a multicolor astigmatism mask vs that of a single color one. The single hole is imaged at 5 different defocus positions (z values) throughout a 1μm z range (-0.5,-0.25,0,0.25,0.5) μm, 500 frames at each position, under the same imaging conditions. The source is localized in 3D at each frame, using the ThunderSTORM [13] plugin in FIJI [14], with suitable calibration measurements. Figure S17 shows the precision at each position for the two masks, defined as the standard deviation of all points at a given z position. As expected, the single-color PSF somewhat outperforms the multicolor one, with the mean (x,y,z) precision ratios being (84%,80%,84%).
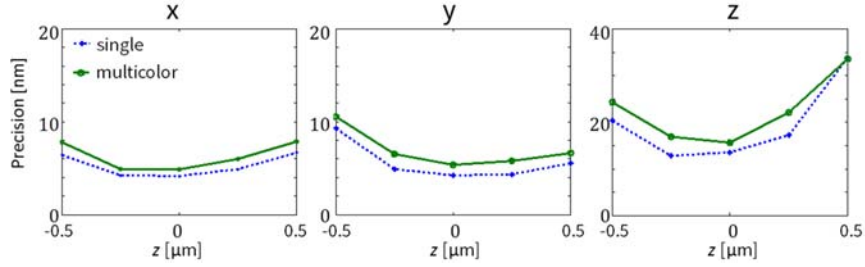
Supplemental Figure S17 | single color astigmatism vs. multicolor astigmatism precision. Results of x,y,z precision measurements (500 localized frames at each z position), using nanohole filled with Alexa647.

Point source fitting

In the thick cell imaging experiment, the Tetrapod PSFs were fit using maximum likelihood estimation (MLE), solved numerically in Matlab. The fitting method is similar to those previously described elsewhere [1], and is based on fitting a region of interest (ROI) to an imaging model, described in the "Optical setup and imaging model" section in this Supplementary Information text.

First, background subtraction is performed, by fitting all pixels in the ROI under a threshold (set as 0.5 of the max intensity pixel) to a 2D polynomial of order 4, and subtracting from the raw image. Then, a step of coarse localization takes place, in which the normalized-correlation between the ROI and a coarsely sampled (z-increments of 250 nm) dictionary of model PSFs is calculated. The normalized-correlation is defined as:

$$NormCor[k] = max_{x_0, y_0} \left| \iint N_{data}(x, y) N_{model,k}(x - x_0, y - y_0) dx dy \right| \tag{12}$$

where $N_{data}(x, y)$ is the normalized raw data, namely $N_{data} = I_{data} / || I_{data} ||$, and similarly, $N_{model,k}$ is the normalized model image, for defocus k. Here, I_{data} is the raw data, after background subtraction, converted to units of photons (rather than camera counts). The output of this step is the maximally correlative dictionary element, namely, *arg max(NormCor[k])*.

The next step is a more precise MLE fit, using the coarse estimation as initial point. Given an imaging model and a noise model, it is possible to calculate the likelihood of a measurement given a set of underlying parameters [15, 16]. The set of parameters we seek in each frame is the five element vector ($x,y,z,$N$,\beta$) comprising the 3D position of the emitter, the total signal photons, and the mean background level, respectively. The estimated parameters are found by seeking the maximum of the likelihood function. In practice, the negative log-likelihood (LL) is minimized, assuming each pixel of the image is corrupted by Poisson noise. The appropriate objective function is thus given by [16]:

$$LL(\mathbf{\mu};I) = \sum_{x,y} \mu(x,y) - I(x,y) \ln[\mu(x,y)] + C \tag{13}$$

Where $I(x,y)$ is the number of photons detected in pixel x,y of the measured image, $\mu(x,y)$ is the expected number of photons in pixel x,y, computed using the parameters we wish to optimize, and C is an additive term which does not affect the minimization. The minimization of the LL is performed in this work by Matlab's fmincon function. Astigmatic PSFs – namely, super-resolution data and precision experiments, were fit using the ThunderSTORM [13] plugin for FIJI [14]. Calibration measurements were taken by axially scanning a nanohole filled with Alexa647 dye (same as used in Fig. S8).

The elongated PSFs used for two-color simultaneous imaging of microtubules and mitochondria in B-SC-1 cells (main text Fig. 4) were fit using 2D Gaussian fitting to determine the lateral position. Background subtraction was performed by pixelwise median filtering over 100 frames. The emitter color was classified using the elongation direction of the PSF, more specifically, by the ratio between the standard deviations in the x and y direction. The selection threshold was determined from a nanohole array calibration measurement. Fig. S18 shows the ratio of standard deviations of a full field of view of nanohole localizations, from 100 frames of green laser excitation (in green) and 100 frames of red laser excitation (in red). As can be seen in the figure, the colors are distinguishable by this ratio (threshold=1.1).
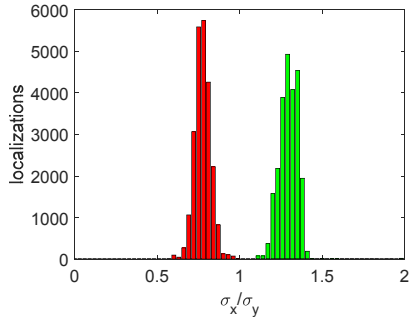
Supplemental Figure S18 | Red/green elongation ratios from nanohole array measurements.

Localization precision

Theoretical and numerical analysis

A matter of paramount importance to localization microscopy is the experimental precision with which the 3D position of a fluorescent emitter may be determined. The Cramer-Rao lower bound (CRLB) is a metric that provides the best theoretically achievable localization precision, given a fixed photon budget and fluorescence background [17]. In our previous work [18], we designed *optimized* PSFs by minimizing the CRLB with respect to the phase mask pattern loaded on the spatial light modulator. In this section, we use CRLB calculations to benchmark the performance of our optimized, dual-color 20 μm Tetrapod PSF, and compare with experimentally measured localization precision.

Using the method described previously in [1, 18], we calculated the CRLB associated with the Tetrapod PSF, for a range of experimentally relevant signal photon levels, and a background of 50 photons per pixel. All calculations were carried out using a simulated microscope defocus of 3 μm, for an emitter at a water-glass interface. The CRLB associated with both green ($\lambda = 559$ nm) and red ($\lambda = 699$ nm) emitters was determined. In addition, we simulated a corpus of noisy images using photon shot-noise (Poisson) statistics, and used maximum likelihood estimation to estimate emitter position from 100 simulated images. Standard deviations in simulated emitter localizations were determined. We define this standard deviation as our localization precision.

In Fig. S19 we plot the results of our CRLB calculations, in addition to the standard deviations in position measurements achieved when localizing simulated images. The close agreement between the CRLB calculations and the localization precision achieved when

28

estimating positions of simulated images demonstrates that our algorithm used for estimating emitter position makes efficient use of detected photons.

In measurements conducted using the dual-color Tetrapod PSF, our experimental localization precision (20 – 40 nm) was degraded by a factor of two to three, relative to the theoretical precision predicted using the CRLB. We ascribe this discrepancy to the following factors: Firstly, optical aberrations are not accounted for using our localization algorithm. Since our imaging model does not perfectly match experimentally acquired data, we do not expect the CRLB to be met. Careful measurement of optical aberrations and inclusion into the imaging model used for emitter localization is currently a subject of substantial interest and an active area of research [19, 20]. Secondly, the use of a high electron-multiplication gain setting (EM gain of 200) on our image sensor distorts photon shot-noise statistics, causing the variance of measured signals to increase and localization precision to decline accordingly [21, 22]. Finally, the fluorescence background of our experimentally acquired images is slightly non-uniform, leading to an additional source of model-mismatch.
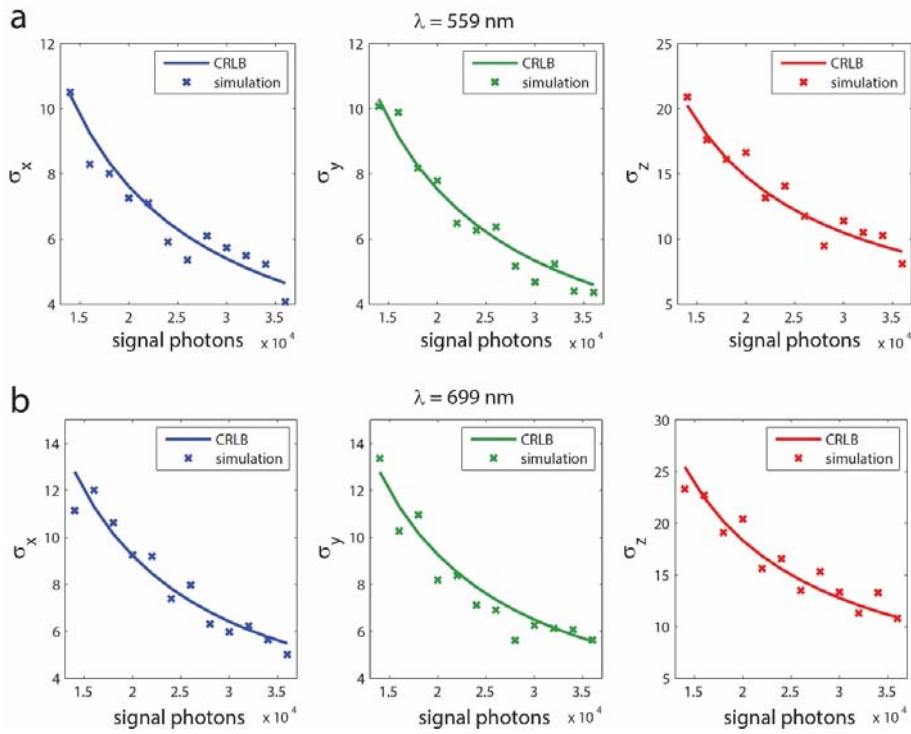
Fig. S19 | CRLB of the dual-color 20 μm Tetrapod PSF. a, CRLB (in nm) as a function of signal photons for a green emitter (λ = 559 nm). A uniform background of 50 photons per pixel was included in all calculations. Additionally, we report the localization precision (in nm) achieved from simulated noisy images. Each point is computed from the standard deviation of position measurements obtained from 100 simulated images. **b,** Calculations were repeated for a red emitter (λ = 699 nm) using the same PSF design, (i.e. the same voltage map applied to the SLM).

Experimental precision estimation

In order to estimate the localization precision in the tracking experiment, a sample consisting of immobilized red and green microspheres (by spin-coating in 1.5% PVA) on a glass cover-slip was used. Two microspheres were imaged separately, at 3 defocus positions (-3,0,3 μm), covering a 6 μm range in which the microspheres were diffusing. A set of 200 images were taken at each defocus position for each microsphere.

Intensities of the illuminating lasers (514 nm and 641 nm) were set such that the total number of photons per frame per bead is similar to the experimental diffusion data (green mean ~18k, red mean ~34k). In addition, white light was added to serve as background noise, to match the experimental background level (mean ~40 photons per pixel).

Each microsphere was localized in each frame, yielding 3D distributions of localization coordinates (x,y,z). The resulting distributions are given in Fig. S17. The mean precision, defined as the standard deviation throughout the z range of for the green microspheres was (20 nm, 23 nm,45 nm) in (x,y,z). For the red bead the mean precision was: (12 nm, 13 nm, 39 nm).
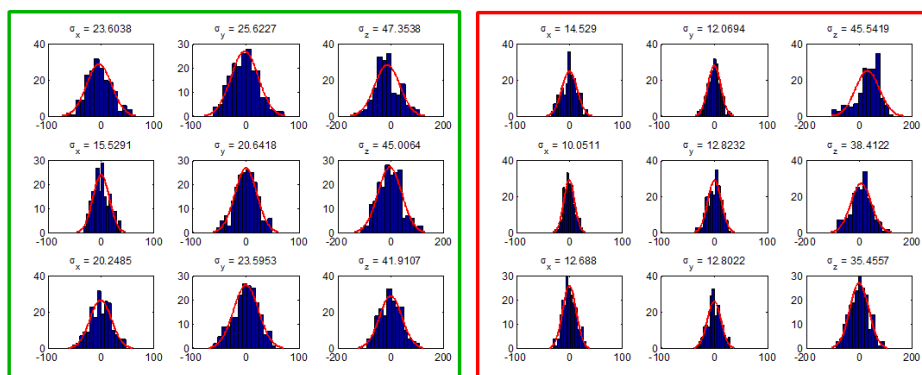
Supplemental Figure S20 | Experimental precision: Tracking fluorescent particles over extreme depth ranges. Histogram of localized immobilized green and red microspheres (Left and right, respectively), over a 6 μm *z*-range (-3,0,3 μm) shown on top row, middle row, and bottom row, respectively. x-axis units are in nm, y-axis units are in counts. Standard deviations of each histogram is given on top, in nm. Mean standard deviations over entire range: (12 nm, 13 nm, 39 nm).

To estimate the localization precision of the fiducial in the 3D super-resolution experiment (SI section "3D Super-resolution imaging"), the fiducial was localized for 500 frames when the focus was at the top of the cell, and for 500 frames when the focus was at the bottom of the cell. During those time the focal plane was relatively static, and to compensate for drift, a linear fit of the localization vs. time was subtracted from the measurements. The resulting (x,y,z) localization histograms are shown in Fig. S21. The mean fiducial (x,y,z) localization precision (mean x,y,z standard deviations) is: (10 nm, 8 nm, 14 nm).
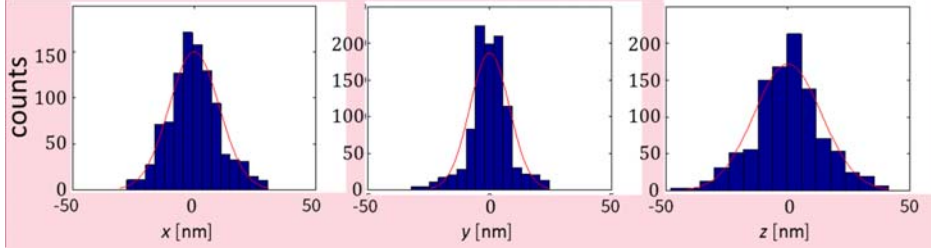
31

Supplemental Figure S21 | Experimental precision: Fiducials for 3D imaging. Repeated localizations (1000 frames) of a fiducial microsphere, focusing on the bottom of the cell and on the top of the cell. *x,y,z* localization results are shown (left, center, right), exhibiting a standard deviation of (10 nm, 8 nm, 14 nm) respectively.

Dielectric multicolor mask

A controllably-multicolor PSF can be obtained by using optical elements other than LC-SLM. To demonstrate this, we designed, fabricated and tested a dielectric (quartz) phase mask that modulates different wavelengths differently, exhibiting controllable, color-dependent PSFs.

Dielectric mask design

The design method works as follows: First, we determine the number of quantization levels, corresponding to possible etch depths. Then, we seek the optimal quantization step size such that the mask produces the closest desired phase delays for the different wavelengths. To do so, we solve the following optimization problem, similar to Eq. 6:

$$d_{xy} = argmin \sum_{i=1}^{N} Dist_{2\pi} \left(P_i\left(d_{xy}\right), D_{xy,i} \right)^2 \tag{14}$$

where d_{xy} is the etching depth in position x,y, $D_{xy,i}$ is the desired phase delay in position x,y, $Dist_{2\pi}$ denotes phase distance as in Eq. 5, and $P_i(d)$ is the phase delay experienced by wavelength λ_i for an etching depth d, given by: $P_i(d) = \frac{2\pi d}{\lambda}[n(\lambda)-1]$, with n being the refractive index of the mask material (quartz [23]).

To demonstrate the applicability of the method, we designed a mask such that green and red emitters (mean emission wavelengths = 542 nm and 673 nm) exhibit astigmatic PSFs with principal axes rotated by 45°.

Dielectric mask fabrication

We used standard photolithography methods in the Stanford Nanofabrication Facility on 4-inch quartz wafers (100 mm in diameter, and 475-475 μm in thickness, produced by WRS Materials) to fabricate the transmissive fixed dielectric phase mask [24].

The quartz wafers were first cleaned in a chemical bath of piranha solution (90% sulfuric acid, 10% hydrogen peroxide) at 70°C for 20 min. The wafers were then rinsed with clean water in an automatic dump rinser and a spin/rinse dryer. Next, the wafers were placed in a Yield Engineering Systems (YES) oven to be dehydrated at 150°C before being primed with hexamethyldisilazane (HDMS). The HDMS allows for better coverage and adhesion between the wafer and the photoresist in the next step. After being primed, the wafers were spin coated with a 1.6 μm thick layer of Shipley 3612 positive photoresist with 5 mm edge bead removal by using a Silicon Valley Group (SVG) resist coat system. Next, the wafers were pre-baked on a hot plate at 90°C for 120 seconds to drive off excess solvent and to turn the photoresist from a liquid form into a film.

The photoresist film was patterned by exposure to UV illumination with a KarlSuss MA-6 aligner for 1.6 seconds. The patterns on the binary masks used in the exposure step were designed by converting the multicolor mask into four different binary masks (4 bits = 16 levels). The four binary mask patterns were printed by a vendor. After exposure, the photoresist on the wafers was then baked on a hot plate at 110°C for 90 seconds to set the photoresist. The wafers were then placed on a SVG developer to remove the positive photoresist in the exposed regions. Next, the wafers were placed in a 90°C oven for 20 min to drive off moisture and harden the photoresist.

Finally, the quartz wafers are placed in an Applied Materials Precision 5000 Etcher to be etched with the magnetically-enhanced reactive ion etch (MERIE) system. The duration of the etching period was calibrated and adjusted for each step height. After the etching step, the photoresist on the wafers was stripped with a Gasonics aura plasma asher. In addition to using the plasma system to strip the photoresist, the wafers were placed in a chemical bath of PRS-3000 at 60°C for 20 min.

The wafers were then rinsed with clean water in an automatic dump rinser and a spin/rinse dryer. After stripping away all of the photoresist, the quartz wafers were characterized with a Sensofar S Neox 3D optical profiler. This tool uses white-light vertical scanning interferometry to

measure the step heights. After confirming the step heights, the entire process is repeated again starting at the HDMS priming step until all etch steps were completed with the four different binary masks. The designed multicolor astigmatic mask, as well as an interferometric surface profile scan of the fabricated mask is shown in Fig. S22. The fidelity of the process is reasonably good, although there are places at the edge transitions where the fabrication can be improved.
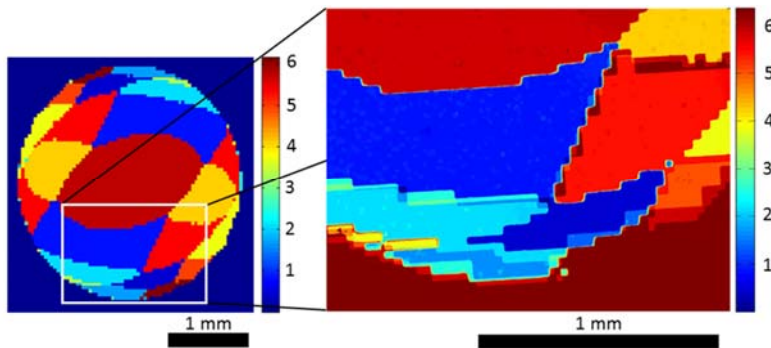
Supplemental Figure S22 | Designed and fabricated dielectric mask. The design of the two-color astigmatic mask (left) and the interferometric surface profile scan of the fabricated quartz phase mask (right). Color bars represent the designed and measured etch depth in microns.

Dielectric mask PSF measurements

We imaged a sample of mixed red and green microspheres in PVA on a cover slip. Fig. S23 shows a stack of images of two microspheres (red and green), obtained by scanning over a 1.4 µm range in z. The 45° rotation between the axes of the red and green astigmatic PSFs is apparent in the figure.

$z = -0.5$ µm $z = -0.2$ µm $z = 0.1$ µm $z = 0.5$ µm
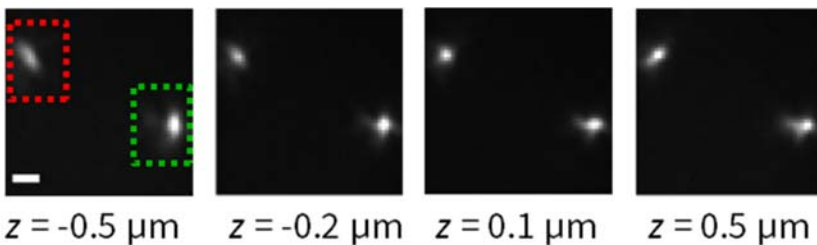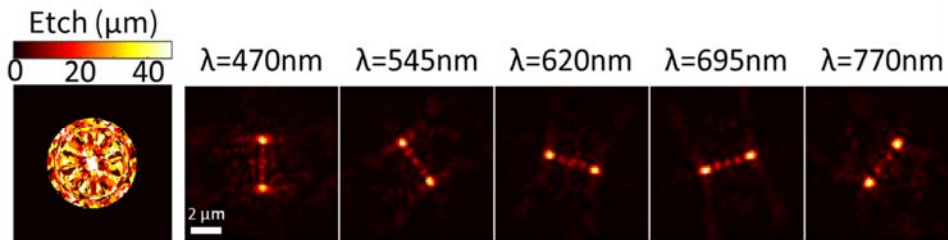
Supplemental Figure S23 | Multicolor dielectric z-scan. A red and green microsphere (shown in red and green boxes) imaged simultaneously over a 1.4 µm z range, using the fabricated dielectric mask in the Fourier plane. Scale bar = 1 µm.

34

Potential of multicolor dielectric masks

Using a dielectric mask for generating a multicolor PSF has two key advantages over a LC-SLM. First, it has larger transmittance, leading to higher signal. Second, it has the potential for much larger 'dispersion', namely, with thick etching, one can design a phase modulating mask with significant spectral dependence.

Here we demonstrate the power of the dielectric mask approach by using our design method to numerically generate a mask capable of modulating 5 wavelengths within the visible range. The PSF is a rotated 6 μm Tetrapod, with rotation angles of 0,36,72,108, and 144 degrees, selected to avoid degeneracy of the PSFs throughout the z range of the PSFs. The mask and the resulting PSFs for an emitter defocused by 3 μm are shown in Fig. S24.

The mask was designed according to specific fabrication constraints, comprising of 256 etching steps (185 nm each), for a total etching depth of 47.175 um. The physical pixel size (pitch) of the mask is 29 um.

Supplemental Figure S24 | Multicolor dielectric mask for 5 colors. A dielectric mask (left) designed to modulate 5 different wavelengths in a 300 nm range, in a rotated 6 μm Tetrapod PSF. The calculated PSFs of a 3 μm defocused emitter for the different wavelengths are shown on the right.

References

1. Y. Shechtman, L. E. Weiss, A. S. Backer, S. J. Sahl, and W. E. Moerner, "Precise 3D scan-free multiple-particle tracking over large axial ranges with Tetrapod point spread functions," Nano Lett. **15,** 4194-4199 (2015).

2. B. Richards and E. Wolf, "Electromagnetic Diffraction in optical systems. II. Structure of the image field in an aplanatic system," Proc. R. Soc. London Ser. A **253,** 358-379 (1959).

3. D. Axelrod, "Fluorescence excitation and imaging of single molecules near dielectric-coated and bare surfaces: a theoretical study," J. Microsc. **247,** 147-160 (2012).

4. J. W. Goodman, *Introduction to Fourier Optics* (Roberts & Company Publishers, 2005).

5. Anonymous *User Manual, XY Phase Series Spatial Light Modulators* (Boulder Nonlinear Systems, Inc., 2010).

6. A. von Diezmann, M. Y. Lee, M. D. Lew, and W. Moerner, "Correcting field-dependent aberrations with nanoscale accuracy in three-dimensional single-molecule localization microscopy," Optica **2,** 985-993 (2015).

7. S. Cox, E. Rosten, J. Monypenny, T. Jovanovic-Talisman, D. T. Burnette, J. Lippincott-Schwartz, G. E. Jones, and R. Heintzmann, "Bayesian localization microscopy reveals nanoscale podosome dynamics," Nat. Methods **9,** 195-200 (2012).

8. Y. Shechtman, S. Gazit, A. Szameit, Y. C. Eldar, and M. Segev, "Super-resolution and reconstruction of sparse images carried by incoherent light," Opt. Lett. **35,** 1148-1150 (2010).

9. S. J. Holden, S. Uphoff, and A. N. Kapanidis, "DAOSTORM: an algorithm for high- density super-resolution microscopy," Nat. Methods **8,** 279-280 (2011).

10. L. Zhu, W. Zhang, D. Elnatan, and B. Huang, "Faster STORM using compressed sensing," Nat. Methods **9,** 721-723 (2012).

11. A. Barsic, G. Grover, and R. Piestun, "Three-dimensional super-resolution and localization of dense clusters of single molecules," Sci. Rep. **4,** (2014).

12. J. Huang, M. Sun, K. Gumpper, Y. Chi, and J. Ma, "3D multifocus astigmatism and compressed sensing (3D MACS) based superresolution reconstruction," Biomedical optics express **6,** 902-917 (2015).

13. M. Ovesny, P. Krizek, J. Borkovec, Z. Svindrych, and G. M. Hagen, "ThunderSTORM: a comprehensive ImageJ plug-in for PALM and STORM data analysis and super-resolution imaging," Bioinformatics **30,** 2389-2390 (2014).

14. J. Schindelin, I. Arganda-Carreras, E. Frise, V. Kaynig, M. Longair, T. Pietzsch, S. Preibisch, C. Rueden, S. Saalfeld, and B. Schmid, "Fiji: an open-source platform for biological-image analysis," Nature methods **9,** 676-682 (2012).

15. S. M. Kay, *Fundamentals of Statistical Signal Processing: Estimation Theory* (Prentice-Hall PTR, 1993).

16. A. V. Abraham, S. Ram, J. Chao, E. S. Ward, and R. J. Ober, "Quantitative study of single molecule location estimation techniques," Opt. Express **17,** 23352-23373 (2009).

17. R. J. Ober, S. Ram, and E. S. Ward, "Localization accuracy in single-molecule microscopy," Biophys. J. **86,** 1185-1200 (2004).

18. Y. Shechtman, S. J. Sahl, A. S. Backer, and W. E. Moerner, "Optimal Point Spread Function Design for 3D Imaging," Phys. Rev. Lett. **113,** 133902 (2014).

19. S. Quirin, S. R. P. Pavani, and R. Piestun, "Optimal 3D single-molecule localization for superresolution microscopy with aberrations and engineered point spread functions," Proc. Natl. Acad. Sci. U. S. A. **109,** 675-679 (2012).

20. S. Liu, E. B. Kromann, W. D. Krueger, J. Bewersdorf, and K. A. Lidke, "Three dimensional single molecule localization using a phase retrieved pupil function," Opt. Express **21,** 29462 (2013).

21. M. Hirsch, R. J. Wareham, M. L. Martin-Fernandez, M. P. Hobson, and D. J. Rolfe, "A stochastic model for electron multiplication charge-coupled devices–from theory to practice," PloS one **8,** e53671 (2013).

22. J. Chao, R. Sripad, E. S. Ward, and R. J. Ober, "Ultrahigh accuracy imaging modality for super-localization microscopy," Nat. Methods **10,** 335-338 (2013).

23. I. Malitson, "Interspecimen comparison of the refractive index of fused silica," JOSA **55,** 1205-1208 (1965).

24. A. Gahlmann, J. L. Ptacin, G. Grover, S. Quirin, A. R. S. von Diezmann, M. K. Lee, M. P. Backlund, L. Shapiro, R. Piestun, and W. E. Moerner, "Quantitative multicolor subdiffraction imaging of bacterial protein ultrastructures in 3D," Nano Lett. **13,** 987-993 (2013).